

Defining and Calculating Self-Helicity in Coronal Magnetic Fields

D.W. Longcope and A. Malanushenko

*Department of Physics, Montana State University
Bozeman, MT 59717, USA*

ABSTRACT

We introduce two different generalizations of relative helicity which may be applied to a portion of the coronal volume. Such a quantity is generally referred to as the self-helicity of the field occupying the sub-volume. Each definition is a natural application of the traditional relative helicity but relative to a different reference field. One of the generalizations, which we term additive self-helicity, can be considered a generalization of twist helicity to volumes which are neither closed nor thin. It shares with twist the property of being identically zero for any portion of a potential magnetic field. The other helicity, unconfined self-helicity, is independent of the shape of the volume occupied by the field portion and is therefore akin to the sum of twist and writhe helicity. We demonstrate how each kind of self-helicity may be evaluated in practice.

The set of additive self-helicities may be used as a constraint in the minimization of magnetic energy to produce a piece-wise constant- α equilibrium. This class of fields falls into a hierarchy, along with the flux constrained equilibria and potential fields, of fields with monotonically decreasing magnetic energies. Piece-wise constant- α fields generally have fewer unphysical properties than genuinely constant- α fields, whose twist α is uniform throughout the entire corona.

Subject headings: MHD — Sun: corona — Sun: magnetic fields

1. Introduction

Plasma astrophysicists have found a broadly useful tool in the quantity of magnetic helicity. In its basic form, magnetic helicity is the integral of $\mathbf{A} \cdot \mathbf{B}$, where $\mathbf{A}(\mathbf{x})$ is the vector potential generating the magnetic field: $\nabla \times \mathbf{A} = \mathbf{B}$. For the quantity to be useful, or even *well-defined*, it is essential that the integral be performed over a “flux enclosed-volume”: a volume on whose surface $\mathbf{B} \cdot \hat{\mathbf{n}} = 0$. Magnetic helicity is conserved under any fluid motions provided the conductivity is very high — a condition almost always satisfied

by astrophysical plasmas. This conservation is related to the fact that magnetic helicity is a topological property: it depends on magnetic field lines and is unchanged by their continuous deformation.

Magnetic helicity, in its basic form, is inapplicable to the solar corona since magnetic field is normal to its lower boundary, $z = 0$, here called the photosphere. To overcome this difficulty Berger & Field (1984) introduced *relative helicity*, defined relative a reference field, $\mathbf{B}_0(\mathbf{x})$, matching the normal components of \mathbf{B} on all of the volume's boundaries. The relative helicity can be found by integrating $(\mathbf{A} + \mathbf{A}_0) \cdot (\mathbf{B} - \mathbf{B}_0)$ over the entire volume (Finn & Antonsen 1985). This modification renders the quantity well-defined while maintaining its property of being conserved under ideal *internal* motions (i.e. motions of a perfectly conducting plasma).

The most common choice¹ for a reference is the potential field, $\nabla \times \mathbf{B}_0 = 0$. Given normal components on all boundaries the potential field is unique and so therefore will be the helicity relative to it. In a volume which is actually flux-enclosed the potential field vanishes identically, so the relative helicity reverts to the basic helicity. More importantly the potential field has the minimum possible magnetic energy for its normal field distribution. A field with non-vanishing relative helicity therefore necessarily has energy above its minimum (free energy). This particular property has much to do with the utility of relative helicity in studies of the coronal magnetic field. It is especially useful since helicity is changed most readily by motions at the boundary, *helicity flux*, which can be observed and quantified (Chae 2001; Démoulin & Berger 2003). It has proven to be far more difficult to observe coronal energy changes directly than to infer them from helicity changes (Chae et al. 2001; Démoulin et al. 2002; Kusano et al. 2002; Nindos et al. 2003; Chae et al. 2004).

To make full use of its energetic implications some recent applications have sought to attribute magnetic helicity (relative helicity) to selected portions of a coronal field such as sheared coronal loops (Kusano et al. 2002; Melrose 2004), newly emerged active regions (Longcope & Welsch 2000), helmet streamers (Low 1994; Zhang et al. 2006), kinking flux ropes (Fan & Gibson 2004; Longcope et al. 2007), or flux ropes ejected from the corona (Rust & Kumar 1994; Démoulin et al. 2002; Dasso et al. 2003). Such attribution must be done with care in order to preserve the meaning of relative helicity. The product $(\mathbf{A} + \mathbf{A}_0) \cdot (\mathbf{B} - \mathbf{B}_0)$ is not an actual density whose integral over any portion of the coronal volume yields the helicity of that portion. It is, in fact, only meaningful if integrated over the volume at whose

¹The potential field is not the only choice in the literature. Low (2006) proposes an elegant new version of relative helicity which is equivalent to $H(\mathbf{B}|\mathbf{B}_0)$ using, as the reference field $\mathbf{B}_0 = \mathbf{B}_s$, one of the components in a generalized Chandrasekhar-Kendall decomposition of $\mathbf{B}(\mathbf{x})$.

boundary the magnetic field and reference fields match.

Trouble with the partial integration of $(\mathbf{A} + \mathbf{A}_0) \cdot (\mathbf{B} - \mathbf{B}_0)$ is presaged by the gauge freedom in choices of the vector potentials. This gauge-dependence disappears only when the dot product is integrated over the entire volume. This seemingly technical issue actually points to a fundamentally physical problem in defining topological characteristics of field lines with end points — in this case photospheric footpoints.

The topological nature of helicity is often illustrated using vivid, but unrealistic, examples where magnetic field is confined to one or more separated closed tubes (Berger & Field 1984; Moffatt & Ricca 1992). In such fields the helicity integral can be rewritten as a sum of two kinds of terms each of which is itself invariant to continuous ideal deformation. The first kind of term, called *mutual helicity*, depends on how pairs of closed tubes are interlinked. It is common intuition that two linked, closed loops cannot be unlinked by simply moving them, distorting them or viewing them from different angles. If the tubes are *not* closed, on the other hand, they might appear linked when viewed from one angle and unlinked when viewed from another or moved appropriately. Linkage in this latter case cannot be meaningfully defined as a topologically invariant characteristic. This same difficulty lies at the heart of defining a meaningful helicity for field lines which end at photospheric footpoints.

In the illustrative example above, the second kind of term, called *self-helicity*, depends on the field within each particular tube. It is this kind of quantity which solar physicists have sought to apply to coronal magnetic fields. It might reveal whether a flux rope erupting from an active region carries with it some “self-helicity”, and whether that will alter the helicity of the active region it erupts from. In the present work we explore methods of rigorously defining such a self-helicity for field lines anchored at photospheric footpoints.

Like any form of relative helicity, the self-helicity of a coronal sub-volume will depend on some reference field. There are at least two natural candidates for a reference field when considering a sub-volume. One is a potential field filling the coronal volume and tangent to its boundaries everywhere except the “feet” of the sub-volume. A second is a field confined to the sub-volume which is current-free except where it abuts the surrounding corona. Each choice yields a well-defined helicity which might legitimately be called the self-helicity of the sub-volume. The two different choices, however, produce different quantities with different properties. In this work we consider both in turn and explore their properties. We find that the second form, while harder to compute in practice, coincides more with intuition and therefore promises more insight into coronal magnetic fields.

The second definition of self-helicity is also distinguished by the fact that it can be used to generalize the constant- α equilibrium. It has long been known that force-free fields,

$\nabla \times \mathbf{B} = \alpha \mathbf{B}$, whose twist α is uniform, called *constant- α equilibria*, are the fields of the minimum possible magnetic energy given their helicity (Woltjer 1958) or relative helicity. This property is physically relevant because helicity is changed less than is energy by non-ideal processes, such as resistivity or fast magnetic reconnection (Berger 1984). Thus internal, non-ideal restructuring can change the topologies of its individual field lines through reconnection, but will not much affect the plasma’s overall relative helicity. By lowering its energy without changing its helicity, this internal restructuring will drive the magnetic field toward a constant- α state (Taylor 1974; Bellan 2000).

The tendency toward a constant- α equilibrium has been experimentally verified in laboratory plasmas (Taylor 1974), but is more problematic in the solar corona. Constant- α fields with any value other than $\alpha = 0$ (i.e. a potential field) will not decay with distance in unbounded volumes. They will therefore have infinite energy and helicity, and are not physically relevant (Seehafer 1978). Nor is it obvious that a field filling an unbounded domain would ever have time enough to restructure all of its field lines in order to “distribute” α uniformly (Low 1994). Instead it seems more reasonable that restructuring within a certain sub-volume of the coronal field will seek to make α constant only within that sub-volume (Wolfson et al. 1994). The result might be a field where α is uniform within separate sub-volumes, but where those α ’s do not necessarily match: α is *piece-wise-constant*. Such fields can behave more realistically in an unbounded volume if, for example, the unbounded portion of the field is potential.

In the present work we demonstrate that a piece-wise constant- α field has the least possible energy given all the different self-helicities in its different sub-volumes. The need for some measure of self-helicity in order to motivate this kind of partially relaxed magnetic field was anticipated by Low (1996). This property follows only when one of the two possible definitions of self-helicity is used. Furthermore, the reference field used in its definition along with an entirely different kind of field, called flux constrained equilibrium (Longcope 2001), are two elements in a hierarchy of fields. This hierarchy, organized by decreasing magnetic energies, also includes the original field \mathbf{B} (at the top), the piece-wise-constant- α field (immediately below it) and the potential field (at the bottom). Such a hierarchy of related magnetic fields could prove useful in estimating free magnetic energies of complex coronal fields from observations. It clearly points to which types of observations will help in the estimation of energy.

Before undertaking this exploration we note that some previous literature has used the terms “self-helicity” and “mutual helicity” in ways inconsistent to the ones we will propose. Berger (1999) and Régnier et al. (2005), for example, use a “mutual helicity” defined as the cross term between the potential and non-potential components of the field, integrated over

the entire volume (i.e. the dot product between the vector potential of one and the magnetic field of the other). Low (2006) generalizes that method to a “two-flux” decomposition into components, each representable by Euler potentials. In either case the “mutual helicity” is well defined, but since both components occupy the same volume it does not provide the distinction we seek. One cannot, for example, use it to quantify the helicity content of an erupting flux rope.

More recently Démoulin et al. (2006) have extended the topological insight provided by isolated flux tubes to define mutual helicity for sets of field lines with photospheric footpoints. Their definition is elegant and (remarkably) independent of reference field. The method as it presently stands applies to individual field lines and not to coronal field filling volumes.

There have been similar attempts to decompose the helicity changes due to motions of the photospheric boundary. This change is found from an integral of the quantity $2(\mathbf{A}_0 \cdot \mathbf{v})(\mathbf{B} \cdot \hat{\mathbf{n}})$. As with the relative helicity itself, this integrand is not a density, and is meaningful only when integrated over the entire photospheric surface. In common situations, the integrand exhibits areas of both signs which cancel on integration, and therefore represent no physical effect. Pariat et al. (2005) found a variant on the integrand which tends to be free of such artifacts and promises to provide useful insight into the origins of coronal helicity.

For photospheric field consisting of isolated flux concentration its is possible to meaningfully decompose the helicity flux integral into terms of two different types (Berger 1984; Longcope et al. 2007). These two categories, termed *spin* and *braiding*, depend respectively on internal motions within a concentration and motions of the concentrations about one another. While similar to the distinction drawn between self-helicity and mutual helicity, they are not necessarily related to one another. If coronal field lines connect one concentration to multiple opposing concentrations, as they almost always do, the two distinctions cannot be meaningfully related to one another — there are not even the same number of “selves” to be assigned helicities as helicity changes. This subtlety is confused by the occasional use, in the literature, of the terms “self” and “mutual” to the boundary flux contributions more properly termed “spin” and “braiding” (Welsch & Longcope 2003).

In this work we use the two most natural definitions of reference field in the standard formula for relative helicity. In the next section we briefly review the definition of relative helicity and the several formulae commonly used to compute it. The following section presents detailed descriptions of the two possible kinds of reference field for a sub-volume. Using them in the formulae for relative helicity yields two different versions of self-helicity which we call *unconfined self-helicity* and *additive self-helicity*. Each is well defined by itself, but they are not equivalent. Section 4 describes methods for computing self-helicities of

each kind in practice. The methods are demonstrated on a quadrupolar field, and shown to yield similar, but not identical, values. Section 5 shows that using additive self-helicity as a constraint in variation of magnetic energy results in a force-free equilibrium whose twist parameter α is uniform within sub-volumes. This *piece-wise-constant- α* field has many advantages over a traditional constant- α field. Among these, it falls in a hierarchy of magnetic fields of decreasing energy which might be used to model a given coronal field. We conclude with a discussion of possible uses to which each kind of self-helicity might be put.

2. Relative Helicity

We will consider a magnetic field $\mathbf{B}(\mathbf{x})$ defined everywhere within a coronal volume \mathcal{V} . Computing its relative helicity (Berger & Field 1984) requires a reference field, $\mathbf{B}_0(\mathbf{x})$, defined over the same volume and matching the normal component of \mathbf{B} along the surface, $\partial\mathcal{V}$. The relative helicity is then defined as (Berger & Field 1984)

$$H(\mathbf{B}|\mathbf{B}_0) \equiv \int_{\mathcal{V}} \mathbf{B} \cdot \mathbf{A} \, d^3x - \int_{\mathcal{V}} \mathbf{B}_0 \cdot \mathbf{A}_0 \, d^3x \quad , \quad \hat{\mathbf{n}} \times (\mathbf{A} - \mathbf{A}_0) = 0 \text{ on } \partial\mathcal{V} \quad (1)$$

where $\mathbf{A}(\mathbf{x})$ and $\mathbf{A}_0(\mathbf{x})$ are vector potentials generating $\mathbf{B}(\mathbf{x})$ and $\mathbf{B}_0(\mathbf{x})$ respectively. The gauge freedom in these vector potentials must be used to make their tangential components match at the outer surface.

The most common volumes used in solar physics are either the half space $z > 0$, $\mathcal{V} = \mathcal{Z}_+$, or a Cartesian box $\mathcal{V} = \mathcal{B} = (0, L_x) \times (0, L_y) \times (0, L_z)$. In both cases we assume the flux crosses only the bottom surface, $z = 0$. When considering the entire half-space ($\mathcal{V} = \mathcal{Z}_+$) it is necessary to require the field to decay sufficiently rapidly with distance that integrals converge, $r^2|\mathbf{B}| \rightarrow 0$ as $r \rightarrow \infty$, for example. Numerical computations cannot, however, be performed over an infinite volume and often use a computational box, $\mathcal{V} = \mathcal{B}$, with “conducting” boundaries (i.e. $\mathbf{B} \cdot \hat{\mathbf{n}} = 0$) on all walls except the bottom. We consider here these two cases at once, but restrict ourselves to these alone.

The relative helicity can be considered as the helicity of an flux-enclosed field constructed using $\mathbf{B}(\mathbf{x})$ in \mathcal{V} above the photosphere and a mirror reflection of $\mathbf{B}_0(\mathbf{x})$ within a mirror image of \mathcal{V} below (Berger & Field 1984). This construction is permitted by the matching vertical components of \mathbf{B} and \mathbf{B}_0 and the horizontal components of \mathbf{A} and \mathbf{A}_0 at the surface of contact ($z = 0$). The integral of $\mathbf{A} \cdot \mathbf{B}$ over the larger volume ($z > 0$ and $z < 0$) is equal to the expression in (1).

A bit of manipulation and use of the fact that $\hat{\mathbf{n}} \times (\mathbf{A} - \mathbf{A}_0) = 0$ on $\partial\mathcal{V}$ permits expression

(1) to be rewritten in the Finn and Antonsen form (Finn & Antonsen 1985)

$$H(\mathbf{B}|\mathbf{B}_0) = \int_{\mathcal{V}} (\mathbf{B} - \mathbf{B}_0) \cdot (\mathbf{A} + \mathbf{A}_0) d^3x \quad . \quad (2)$$

It can be easily verified that the Finn-Antonsen expression is unaffected by independent gauge transformations of the two vector potentials. They may therefore be computed independent of one another and need not match at $\partial\mathcal{V}$, in contrast to the potentials used in expression (1).

It is also possible to generalize expression (1) to cases with unrelated vector potentials by the addition of one surface term

$$H(\mathbf{B}|\mathbf{B}_0) \equiv \int_{\mathcal{V}} \mathbf{B} \cdot \mathbf{A} d^3x - \int_{\mathcal{V}} \mathbf{B}_0 \cdot \mathbf{A}_0 d^3x + \int_{z=0} B_z(x, y, 0) \chi(x, y) dx dy \quad (3)$$

where the scalar field

$$\chi(\mathbf{x}) = \int_{\mathbf{x}_0}^{\mathbf{x}} [\mathbf{A}(\mathbf{x}') - \mathbf{A}_0(\mathbf{x}')] \cdot d\mathbf{l}' \quad , \quad \text{within } z = 0 \quad , \quad (4)$$

arises from introducing a gauge transformation to yield a new version of \mathbf{A}_0 satisfying the condition that $(\mathbf{A} - \mathbf{A}_0) \times \hat{\mathbf{z}} = 0$ on the photospheric surface.

The most common choice of reference field is the potential field $\mathbf{B}^{(v)}$. Defined from the normal field, along with conditions on all boundaries of the volume (we include in this term, the requirement of decay for $\mathcal{V} = \mathcal{Z}_+$.) this field is unique. Thus, if the relative helicity

$$H_R = H(\mathbf{B}|\mathbf{B}^{(v)}) \quad , \quad (5)$$

is not zero the magnetic field *must* have energy above its minimum possible — free magnetic energy.

For the half-space, $\mathcal{V} = \mathcal{Z}_+$, and the particular choice of vector potential

$$\mathbf{A}^{(v)}(\mathbf{x}) = \frac{1}{2\pi} \int_{z'=0} \frac{(\mathbf{x} - \mathbf{x}') \times \hat{\mathbf{z}}}{(x - x')^2 + (y - y')^2} \frac{|\mathbf{x} - \mathbf{x}'| - z}{|\mathbf{x} - \mathbf{x}'|} B_z(x', y', 0) dx' dy' \quad , \quad (6)$$

it can be shown (see DeVore 2000, for example) that $\mathbf{A}^{(v)} \cdot \mathbf{B}^{(v)}$ will integrate to zero. While this means that the second term in expression (1) vanishes, the relative helicity still depends on $\mathbf{A}^{(v)}$ through restriction of \mathbf{A} at the surface.

3. Self-Helicity

For a particular choice of reference field, equations (1), (2) or (3) all yield the same value: the relative helicity of the entire field filling \mathcal{V} . It is less obvious, however, how to define the relative helicity of a portion of that full field: the field within a sub-volume \mathcal{D}_i , we hereafter call a *domain*. We expect there to be several domains, distinguished by subscripts, which together compose the entire volume

$$\bigcup_i \mathcal{D}_i = \mathcal{V} . \quad (7)$$

In the unbounded case, $\mathcal{V} = \mathcal{Z}_+$, at least one of the domains will extend to infinity. Figure 1a shows, in different colors, fields lines from three different domains of a field within $\mathcal{V} = \mathcal{B}$. In this case domains are defined according to which of the photospheric flux regions, from a quadrupole, they connect. The volume \mathcal{D}_i defined by the central connection is depicted in 1b.

Each sub-volume intersects the photosphere at two distinct regions, \mathcal{F}_i^+ and \mathcal{F}_i^- , called footprints (examples are shown in fig. 2). The + or – superscript designates the sign of the vertical field within the footprint. We further assume that the magnetic field \mathbf{B} is tangent to all boundaries, $\partial\mathcal{D}_i$, except for the photospheric footprints. The net magnetic flux in a particular domain can thus be calculated as

$$\int_{\mathcal{F}_i^\pm} B_z dx dy = \pm \psi_i .$$

We define a restricted magnetic field, $\tilde{\mathbf{B}}_i$, which is the magnetic field of the domain alone; $\tilde{\mathbf{B}}_i = 0$ for $\mathbf{x} \notin \mathcal{D}_i$. To facilitate our discussion we introduce the support function

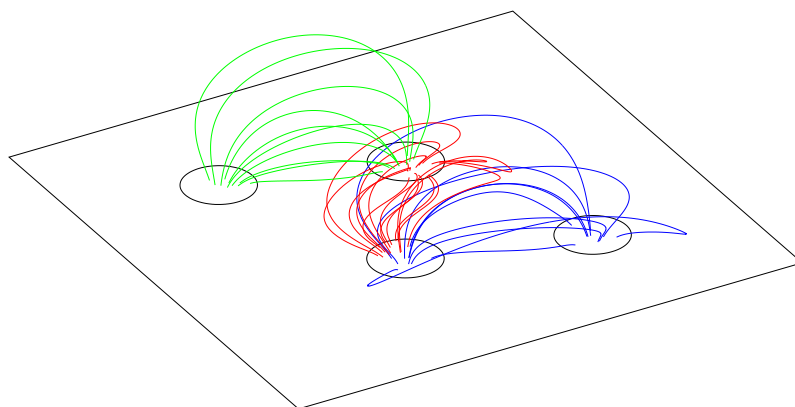
$$\Theta_i(\mathbf{x}) \equiv \begin{cases} 1 & , \quad \mathbf{x} \in \mathcal{D}_i \\ 0 & , \quad \mathbf{x} \notin \mathcal{D}_i \end{cases} . \quad (8)$$

in terms of which $\tilde{\mathbf{B}}_i = \Theta_i \mathbf{B}$. As a result of (7) it is possible to show that

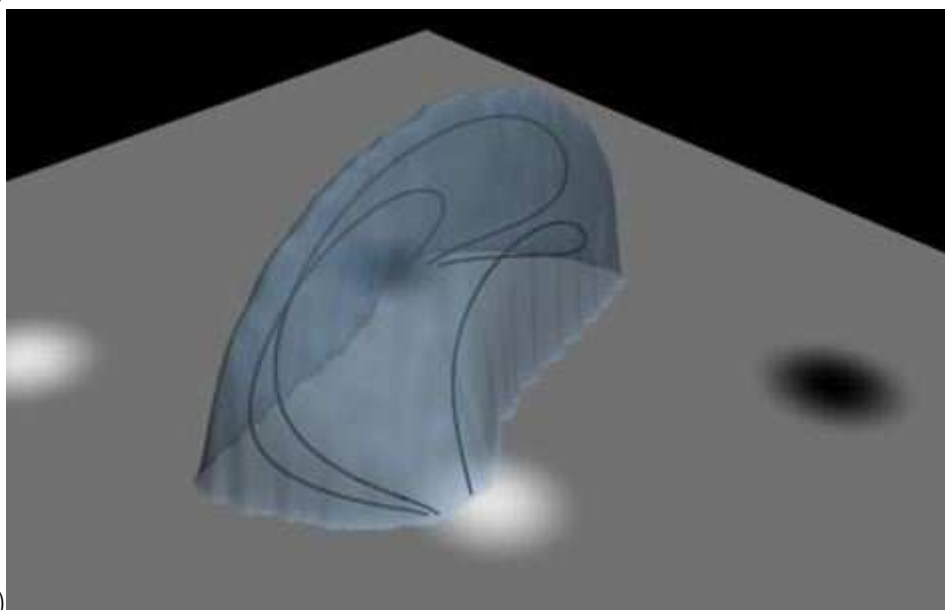
$$\sum_i \Theta_i(\mathbf{x}) = 1 \quad , \quad \sum_i \tilde{\mathbf{B}}_i = \mathbf{B} . \quad (9)$$

The restricted field has tangential discontinuities (i.e. current sheets) at $\partial\mathcal{D}_i$. To see this consider the term $\nabla\Theta_i \times \mathbf{B}$ arising from $\nabla \times \tilde{\mathbf{B}}_i$. The second expression in (9) shows, however, that the artificial boundary current sheets from neighboring domains cancel one another.

The self-helicity of domain \mathcal{D}_i is the relative helicity of $\tilde{\mathbf{B}}_i$. Like any relative helicity this must be defined using a reference field of some kind. There are at least two natural ways to define such a reference field, leading to the two different ways to define self-helicity.



(a)



(b)

Fig. 1.— Perspective views of different domains in a quadrupolar field. (a) Field lines from three different domains defined according to the photospheric flux regions (circles) they interconnect. The domains are $P1-N1$ (red), $P1-N2$ (green) and $P2-N1$ (blue). (b) A transparent rendering of the complete volume enclosing field lines connecting $P1$ to $N1$. A few of the field lines are shown inside the volume. The greyscale at the bottom shows the vertical photospheric field, $B_z(x, y, 0)$. It is smooth, but vanishes outside of the source regions.

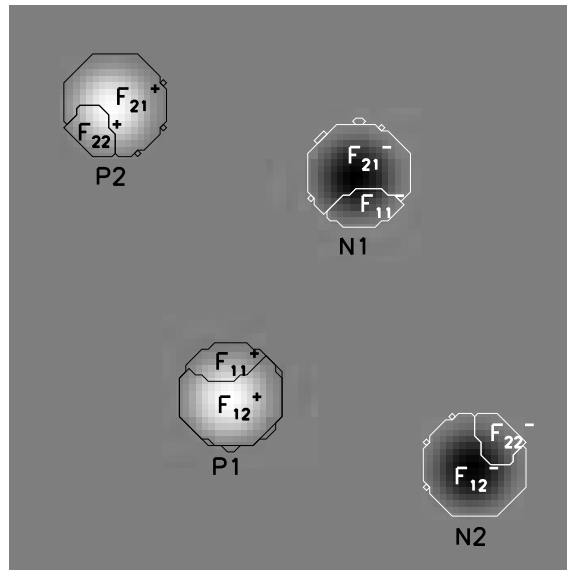


Fig. 2.— The vertical magnetic field B_z (grey scale) for the quadrupolar example field. The four flux sources are labeled $P1, \dots, N2$. The domain of field lines connecting Pi to Nj is called \mathcal{D}_{ij} , and its footprints are labeled \mathcal{F}_{ij}^+ and \mathcal{F}_{ij}^- .

3.1. Self-helicity relative to an unconfined potential field

The first reference field, which we call the *unconfined potential field* $\tilde{\mathbf{B}}_i^{(v)}(\mathbf{x})$, is a potential field matching $\tilde{\mathbf{B}}_i$ at the photosphere. This means that $\hat{\mathbf{n}} \cdot \tilde{\mathbf{B}}_i^{(v)}$ vanishes everywhere on $\partial\mathcal{V}$ except within the footprints, \mathcal{F}_i^+ and \mathcal{F}_i^- . In spite of this photospheric localization $\tilde{\mathbf{B}}_i^{(v)}(\mathbf{x})$ does not vanish outside of \mathcal{D}_i ; it fills the entire coronal volume, as do the vector potentials $\tilde{\mathbf{A}}_i$ and $\tilde{\mathbf{A}}_i^{(v)}$. This and the other magnetic fields introduced in the calculation of the two types of helicities, are summarized in Table 1 and illustrated in fig. 3

field	$\mathbf{B} \neq 0$ in	$B_z \neq 0$	volume currents	surface current
\mathbf{B} magnetic field	\mathcal{V}	$z = 0$	in \mathcal{V}	—
$\mathbf{B}^{(v)}$ potential field	\mathcal{V}	$z = 0$	\times	\times
$\tilde{\mathbf{B}}_i$ restricted field	\mathcal{D}_i	\mathcal{F}_i^\pm	in \mathcal{D}_i	on $\partial\mathcal{D}_i$
$\tilde{\mathbf{B}}_i^{(v)}$ unconfined potential	\mathcal{V}	\mathcal{F}_i^\pm	\times	\times
\mathbf{P}_i confined potential	\mathcal{D}_i	\mathcal{F}_i^\pm	\times	on $\partial\mathcal{D}_i$
$\mathbf{P} = \sum_i \mathbf{P}_i$	\mathcal{V}	$z = 0$	\times	on $\cup_i \partial\mathcal{D}_i$
\mathbf{B}_{α_i} piece-wise constant- α	\mathcal{V}	$z = 0$	\mathcal{V}	on $\cup_i \partial\mathcal{D}_i$

Table 1: A summary of the magnetic fields used in the calculation of self-helicity. The description given in the text is summarized by listing where the field itself is non-zero, where it may have volume current density and where it may have singular surface currents. A dash indicates that currents of that type are not assumed in general circumstances, while a \times indicates that they are forbidden.

The unconfined potential field and corresponding vector potential may be used as a reference in a self-helicity

$$\tilde{H}_i = H(\tilde{\mathbf{B}}_i | \tilde{\mathbf{B}}_i^{(v)}) , \quad (10)$$

which we call the *unconfined self-helicity*. This quantity is the topological difference between

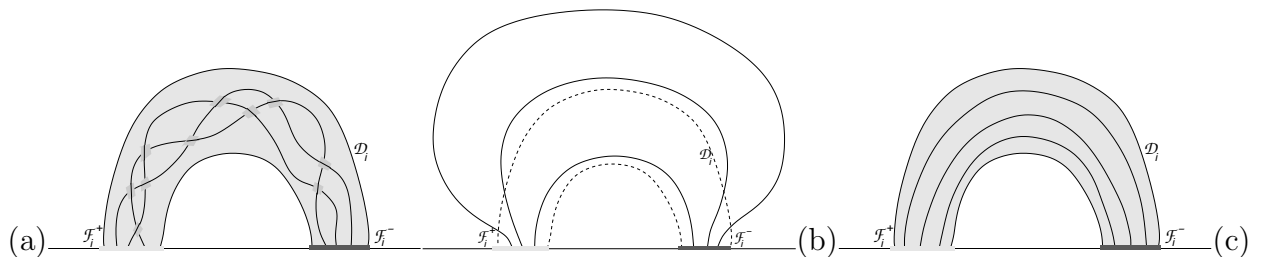


Fig. 3.— Illustration of three fields used in calculations of self-helicity of domain \mathcal{D}_i (grey). (a) The restricted field, $\tilde{\mathbf{B}}_i$. (b) The unconfined field $\tilde{\mathbf{B}}_i^{(v)}$, which extends outside of the domain (dashed). (c) The confined potential field \mathbf{P}_i .

the restricted field and its unconfined, potential counterpart. Owing to the unconfined nature of $\tilde{\mathbf{B}}_i^{(v)}$ and both of the vector potentials, the integral in the Finn-Antonsen form (2), must be performed over the entire volume \mathcal{V} to find the helicity of only \mathcal{D}_i . Alternatively one may use expression (3), and perform the first integral within \mathcal{D}_i , the second over \mathcal{V} and the third within the footprints \mathcal{F}_i^+ and \mathcal{F}_i^- . The gauge field $\chi(x, y)$ is needed only within the footprints, but it must be found using an integral whose path will pass across the photosphere between these. The next section presents a detailed recipe for performing these calculations.

It is instructive to consider the case when the actual field is also the potential field, $\mathbf{B} = \mathbf{B}^{(v)}$. The total relative helicity of the field, (1) clearly vanishes in that case. It is *not* the case, however, that the unconfined, self-helicities of its domains vanish. This follows from the fact that

$$\tilde{\mathbf{B}}_i = \Theta_i \mathbf{B}^{(v)} \neq \tilde{\mathbf{B}}_i^{(v)} .$$

The field on the left, a restriction of the potential field, contains current sheets which confine it to \mathcal{D}_i . If these currents were removed in an artificial evolution without line-tying, the field would expand to fill the whole volume \mathcal{V} . As it does this the footprints of its field lines would, in general, move around within \mathcal{F}_i^+ and \mathcal{F}_i^- . Taking them instead to be fixed within the footprints would over-constrain the problem (Low 2006), leading to a contradiction. Thus we conclude that they must move, and it is this motion which is reflected in \tilde{H}_i . We demonstrate this motion below for a specific example.

3.2. The Additive Self-helicity

The second reference field, which we call the *confined potential field* \mathbf{P}_i , is defined to vanish everywhere outside the domain \mathcal{D}_i as the restricted field $\tilde{\mathbf{B}}_i$ does (see fig. 3c). Since it is a reference field the normal component of \mathbf{P}_i matches that of $\tilde{\mathbf{B}}_i$ on all boundaries. It therefore vanishes everywhere except within the footprints \mathcal{F}_i^+ and \mathcal{F}_i^- ; it is tangent to $\partial\mathcal{D}_i$ everywhere else. It is the field satisfying

$$\nabla \times \mathbf{P}_i = 0 \quad , \quad \nabla \cdot \mathbf{P}_i = 0 \quad , \quad \mathbf{x} \in \mathcal{D}_i \quad , \quad (11)$$

subject to these conditions, and as such is unique.

This reference field is not, however, a truly potential field. Since it vanishes outside the domain, \mathbf{P}_i has current sheets on all the boundaries $\partial\mathcal{D}_i$. These current sheets will, in general, have different current densities than those of the restricted field, $\tilde{\mathbf{B}}_i$; among other differences, the current sheets from neighboring domains do not cancel one another.

Using this second reference field we define a self-helicity of a domain

$$H_i^{(s)} \equiv H(\tilde{\mathbf{B}}_i|\mathbf{P}_i) = \int_{\mathcal{D}_i} (\mathbf{B} - \mathbf{P}_i) \cdot (\mathbf{A} + \mathbf{A}_i^{(p)}) d^3x \quad , \quad (12)$$

where $\mathbf{A}_i^{(p)}$ is the vector potential for \mathbf{P}_i . This corresponds to the helicity of a field following $\mathbf{B}(\mathbf{x})$ within \mathcal{D}_i above the photosphere, and then returning through a reflection of \mathbf{P}_i below. In the special case that the field actually is potential, $\mathbf{B} = \mathbf{B}^{(v)}$, it can be shown that $\mathbf{P}_i = \tilde{\mathbf{B}}_i$ and the self-helicity vanishes. This property, which the unconfined helicity does not share, makes the additive self-helicity particularly intuitive.

The self-helicity integral in (12) is performed only within the domain \mathcal{D}_i . This means that the self-helicities of all domains may be added together. The reference fields also sum together without interference,

$$\mathbf{P}(\mathbf{x}) = \sum_i \mathbf{P}_i(\mathbf{x}) \quad . \quad (13)$$

This reference field is potential within every domain, but has current sheets along all of the separatrices. Each of the vector potentials, $\mathbf{A}_i^{(p)}(\mathbf{x})$, extends outside its own domain, \mathcal{D}_i , but is curl-free there. This means that their sum

$$\sum_i \mathbf{A}_i^{(p)}(\mathbf{x}) = \mathbf{A}^{(p)}(\mathbf{x}) \quad (14)$$

is the vector potential generating $\mathbf{P}(\mathbf{x})$ defined in (13).

The result of these facts is that the additive self-helicities can be summed to yield

$$\sum_i H_i^{(s)} = H^{(s)} = H(\mathbf{B}|\mathbf{P}) \quad . \quad (15)$$

which is itself a relative helicity. This useful property suggests the term *additive self-helicity* for the quantity defined in (12).

The difference between the relative helicity and the total self-helicity is itself a relative helicity

$$H_R - H^{(s)} = H(\mathbf{P}|\mathbf{B}^{(v)}) \equiv H^{(m)} \quad (16)$$

owing to the anti-symmetry of $H(\cdot|\cdot)$ in its two arguments. This means that $H^{(m)}$ is the helicity of the field \mathbf{P} relative to the true potential field, and will vanish in the case that $\mathbf{B}(\mathbf{x})$ is potential since then $\mathbf{B} = \mathbf{P} = \mathbf{B}^{(v)}$. By analogy with the decomposition performed on isolated, closed flux tubes we term this the field's mutual helicity. It is not clear, however, that it can be interpreted simply as the interlinking of the fluxes of the different domains.

3.3. The inequivalence of the self-helicities

The two self-helicities above are different from one another in the sense that they can yield different values for the same restricted field $\tilde{\mathbf{B}}_i$. This is equivalent to the statement that the reference fields have helicity relative to one another

$$H(\mathbf{P}_i|\tilde{\mathbf{B}}_i^{(v)}) \neq 0 \quad , \quad (17)$$

in general. The relative helicity can, once more, be reinterpreted as the traditional helicity of a composite field in a flux-enclosed volume formed by \mathcal{V} above the photosphere, and a mirror image of \mathcal{D}_i below. This volume is filled by $\tilde{\mathbf{B}}_i^{(v)}$ in the upper portion and a reflection of \mathbf{P}_i below. While the normal components of these pieces match across the $z = 0$ plane, their tangential components need not and there will be surface currents in general. Moreover the field lines may link each other leading to a net helicity.

There are particular cases for which the two reference fields have no helicity relative to one another and the two versions of self-helicity agree. One such case is when \mathcal{D}_i has a vertical plane of reflectional symmetry and the normal field within the footprints share this symmetry. Under these circumstances both $\tilde{\mathbf{B}}_i^{(v)}$ and \mathbf{P}_i are reflectionally symmetric and so will be the composite field described above. Such a reflectionally symmetric field has zero helicity so $H(\mathbf{P}_i|\tilde{\mathbf{B}}_i^{(v)}) = 0$ as well. An example of such a case is when \mathcal{D}_i is a section of a torus with a horizontal axis of symmetry (Fan & Gibson 2004). In this case, as with others with the reflectional symmetry just described, both kinds of self-helicity (unconfined or additive) are the same. A distortion of the torus which breaks its symmetry, such as a writhing of its axis, can destroy their equality.

The inequality of the two self-helicities under general circumstances reveals that two common methods of calculating relative helicities in practice are not equivalent. Problems frequently encountered involve a magnetic field defined on a Cartesian computational grid, \mathcal{B} , with five conducting boundaries and some distribution of normal field on the photosphere. It is possible to adopt the view that the box itself is a sub-volume (a domain) $\mathcal{D}_i = \mathcal{B}$, within the entire half space $\mathcal{V} = \mathcal{Z}_+$. Under this view a potential field confined to \mathcal{B} is akin to \mathbf{P}_i and helicity defined relative to it is akin to the *additive* self-helicity. This is sometimes used as the “relative helicity” of \mathbf{B} when invoking eq. (2). A potential field is calculated on the same computational grid, with the same boundaries, and an integral is performed over \mathcal{B} . The alternative is to compute the helicity relative to an unconfined potential field, akin to $\tilde{\mathbf{B}}_i^{(v)}$ here. This version of relative helicity is found by integrating the first term in (1) over \mathcal{B} and using expression (6) for $\mathbf{A}^{(v)}$ so that the second integral vanish (DeVore 2000). We mention this to note that barring a symmetric photospheric flux distribution we expect $H(\mathbf{P}|\tilde{\mathbf{B}}_i^{(v)}) \neq 0$ and these two versions of relative helicity to disagree. For cases where

the flux is concentrated far from the conducting walls the disagreement might, however, be rather small.

4. Calculating the self-helicities

We demonstrate how self-helicities can be calculated in practice using, as examples, constant- α fields in a box, \mathcal{B} , with conducting walls at $x = \pm 1.5$, $y = \pm 1.5$ and $z = 1.5$. The flux distribution at the bottom boundary ($z = 0$) consists of four isolated disks of radius $a = 0.2$, each containing unit flux ($\Phi_0 = 1$) with a smooth profile $\propto (1 - r^2/a^2)^2$. This photospheric distribution is shown in fig. 2 along with labels for the disks. A similar photospheric distribution was used by Longcope & Magara (2004) at the lower boundary of a numerical solution of the full MHD equations. In the present case the axis of the inner, smaller bipole ($P1-N1$, $d = 1$) is tilted by 105° with respect to the outer bipole ($P2-N2$, $d = 2$).

The constant- α field is computed on a uniform $N_x \times N_y \times N_z = 120 \times 120 \times 60$ Cartesian grid. Field lines from the field with $\alpha = -0.7$ are shown in fig. 1. Over the range, $-1 \leq \alpha \leq 1$, the relative helicity of the entire field is very well approximated by α times the coefficient (Démoulin et al. 2002)

$$L_x L_y \sum_{\mathbf{k}} \frac{|\hat{B}_{\mathbf{k}}|^2}{|\mathbf{k}|^3} \simeq 0.373 \quad (18)$$

where $\mathbf{k} = 2\pi(n_x/L_x, n_y/L_y)$ are the wave vectors composing the two-dimensional Fourier space of a doubly-periodic field, and $\hat{B}_{\mathbf{k}}$ are the coefficients in the Fourier expansion of $B_z(x, y, 0)$.

There are four domains in the field, of which fig. 1a shows three. The flux and volume of each domain varies with α in the manner shown in fig. 4. The domain connecting the central sources, $P1$ and $N1$, is much smaller than the other three, which extend to the conducting walls. Its flux increases with α as right-handed twist deflects field lines in a direction favorable to connecting those sources. It is evident in fig. 2 that the left handed twist results in very small footprints, \mathcal{F}_{11}^\pm , skewed counter-clockwise from the opposing source. Increasing α will draw the footprints closer together and makes them larger, so that they enclose a larger flux ψ_{11} .

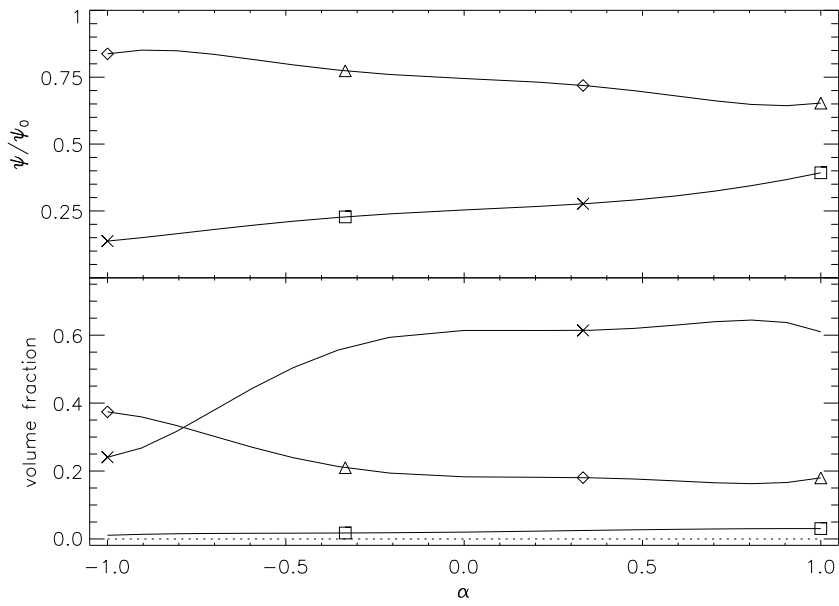


Fig. 4.— The flux (top) and volume (bottom) of the four flux domains. Each domain is given a distinct label: $P1-N1$, square; $P1-N2$, diamond, $P2-N1$, triangle; and $P2-N2$, cross. Due to symmetry some pairs of domains have the same fluxes or volumes, so both symbols appear on the same curve.

4.1. Computing the unconfined helicity.

The unconfined self-helicity can be calculated without explicitly constructing the volume \mathcal{D}_i or the restricted field $\tilde{\mathbf{B}}_i$. If these are available then it will be simplest to construct $\tilde{\mathbf{A}}_i$ throughout \mathcal{V} and use eq. (2) to compute \tilde{H}_i after constructing $\tilde{\mathbf{B}}_i^{(v)}$ and $\tilde{\mathbf{A}}_i^{(v)}$. What is noteworthy is that the same value can be found without knowledge of $\tilde{\mathbf{A}}_i$ except inside \mathcal{D}_i . Moreover, the domain itself can be defined implicitly through the properties of its field lines. We outline below this calculation and henceforth assume only this partial information.

We begin by noting that there exist gauge choices for which $\tilde{\mathbf{A}}_i = \mathbf{A}$ within \mathcal{D}_i . The two vector potentials will certainly differ outside the domain, however, this region is irrelevant in the computation of the first integral in eq. (3),

$$T_1 = \int_{\mathcal{V}} \tilde{\mathbf{B}}_i \cdot \tilde{\mathbf{A}}_i d^3x = \int_{\mathcal{D}_i} \mathbf{B} \cdot \mathbf{A} d^3x . \quad (19)$$

The right-most expression follows from the fact that $\tilde{\mathbf{B}}_i$ vanishes outside \mathcal{D}_i , and from the fact that both $\tilde{\mathbf{B}}_i$ and $\tilde{\mathbf{A}}_i$ agree with their unrestricted counterparts inside.

It is also possible to perform integral (19) without complete knowledge of \mathcal{D}_i , provided it is defined by properties of its field lines such as their connectivity. In this case we rewrite the differential volume element $\mathbf{B} d^3x = d\mathbf{l} d\Phi$ where $d\mathbf{l}$ is the differential line element of a field line and $d\Phi$ is a differential of flux from \mathcal{D}_i . We may then approximate the integral as a sum over field lines, \mathcal{L}_a , randomly selected from \mathcal{D}_i , each representing flux $\delta\Phi$ of the domain,

$$T_1 = \int d\Phi \int \mathbf{A} \cdot d\mathbf{l} \simeq \delta\Phi \sum_a \int_{\mathcal{L}_a} \mathbf{A} \cdot d\mathbf{l} . \quad (20)$$

The random selection may be done by the method of rejection (Press et al. 1986), making the integral relatively easy to compute.

Let us take the case of a domain, such as our example, defined to consist of all field lines linking a pair of photospheric sources. Choose one of the sources, with flux Φ_0 , and generate N random points which sample the photosphere with a probability density proportional to $|B_z|$ within it. Each field line beginning from one of these initial points represents a flux element $\delta\Phi = \Phi_0/N$. While tracing the field line it is easy to perform the line integral in expression (20). If the field line terminates at the designated opposing source it then belongs to \mathcal{D}_i and the line-integral is included in the sum; otherwise it is discarded. The final sum is the Monte Carlo approximation of T_1 .

During the Monte Carlo integration described above it is also possible to compute several

other quantities of interest. For example the net flux and total volume are found by

$$\psi_i \simeq \delta\Phi \sum_a 1 \quad , \quad V_i \simeq \delta\Phi \sum_a \int_{\mathcal{L}_a} \frac{d\ell}{|\mathbf{B}|} \quad , \quad (21)$$

where both sums are performed only when the field line is found to belong to the domain. These methods were used to calculate the fluxes and volumes plotted in fig. 4.

The second integral in expression (3)

$$T_2 = \int_{\mathcal{V}} \tilde{\mathbf{A}}_i^{(v)} \cdot \tilde{\mathbf{B}}_i^{(v)} d^3x \quad , \quad (22)$$

is also easy to compute since the vector potential $\tilde{\mathbf{A}}_i^{(v)}$ can be computed independently of $\tilde{\mathbf{A}}_i$. (Recall that this freedom is not available in expression [1]). When using the half space for the coronal volume, $\mathcal{V} = \mathcal{Z}_+$, one may assume that $\tilde{\mathbf{A}}_i^{(v)}$ is given by expression (6) and therefore take $T_2 = 0$. For the other case, $\mathcal{V} = \mathcal{B}$, one must first compute $\tilde{\mathbf{B}}_i^{(v)}$ within this box. First identify the pixels in \mathcal{F}_i^+ and \mathcal{F}_i^- by tracing field lines from inside each source and recording the ones that end in the designated opposite. In an array containing $B_z(x, y, 0)$, set to zero all but these pixels. Then construct the potential field from this restricted magnetogram in the same fashion $\mathbf{B}^{(v)}$ was found from the entire magnetogram. This is $\tilde{\mathbf{B}}_i^{(v)}(\mathbf{x})$; it will fill \mathcal{V} up to the five conducting walls.

The final term in eq. (3) is an integral over the photospheric surface. The integrand is proportional to $\tilde{B}_z(x, y, 0)$ and will therefore vanish everywhere except within \mathcal{F}_i^+ and \mathcal{F}_i^- . These regions were found explicitly in the previous step, so it is a straightforward task to integrate over each one in turn. The term is

$$T_3 = \int_{\mathcal{F}_i^+} \chi_+(x, y) B_z(x, y, 0) dx dy + \int_{\mathcal{F}_i^-} \chi_-(x, y) B_z(x, y, 0) dx dy - \psi_i \Gamma_+^- \quad , \quad (23)$$

where the scalar fields $\chi_{\pm}(x, y)$ are defined as in eq. (4) except with line integrals beginning at points \mathbf{x}_{\pm} on the footprint perimeters,

$$\chi_+(\mathbf{x}) = \int_{\mathbf{x}_+}^{\mathbf{x}} [\mathbf{A}(\mathbf{x}') - \tilde{\mathbf{A}}_i^{(v)}(\mathbf{x}')] \cdot d\mathbf{l}' \quad , \quad \chi_-(\mathbf{x}) = \int_{\mathbf{x}_-}^{\mathbf{x}} [\mathbf{A}(\mathbf{x}') - \tilde{\mathbf{A}}_i^{(v)}(\mathbf{x}')] \cdot d\mathbf{l}' \quad , \quad (24)$$

and each one following a path confined to its own footprint. For example, χ_+ is found at point \mathbf{x} , in fig. 5 by integrating from point \mathbf{x}_+ along path \mathcal{L}^+ inside \mathcal{F}_i^+ . Recall that $\tilde{\mathbf{A}}_i = \mathbf{A}$ within \mathcal{D}_i , so these potentials will also agree within the footprints. The potentials can be “propagated” to all pixels in the footprint, \mathcal{F}_i^+ , using an algorithm presented by Haffla et al. (2006). The same method is then applied to find χ_- within \mathcal{F}_i^- .

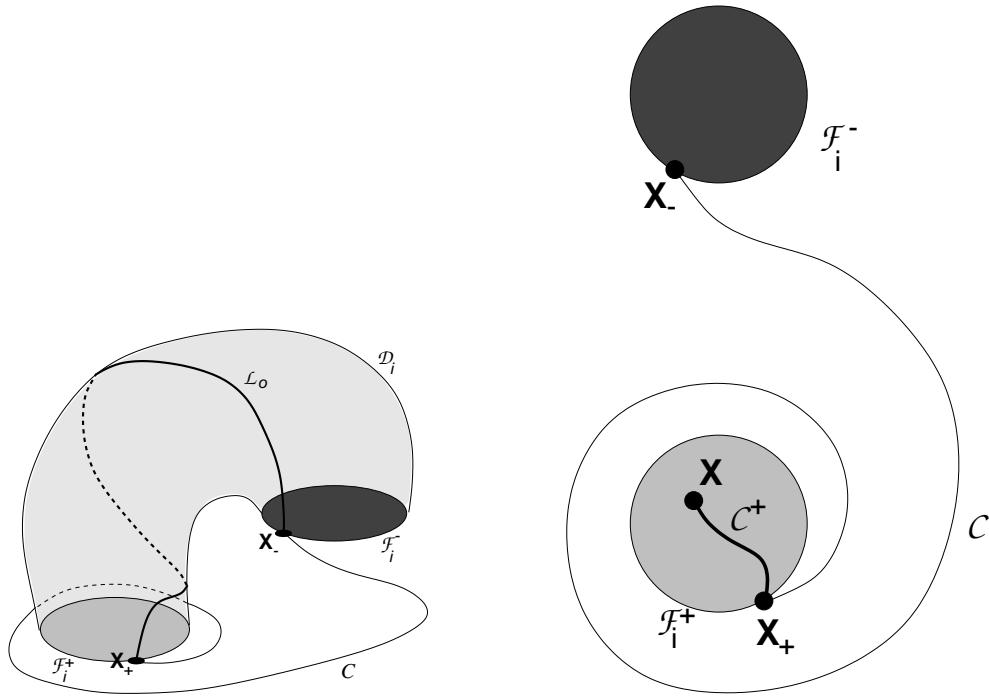


Fig. 5.— Illustrations of the integration paths used in the computation of T_3 for a domain \mathcal{D}_i . A perspective view (left) shows the field line \mathcal{L}_0 on $\partial\mathcal{D}_i$ whose footpoints are \mathbf{x}_+ and \mathbf{x}_- . The fall on the perimeters of the shaded, photospheric footprints \mathcal{F}_i^+ and \mathcal{F}_i^- . This closed along the path \mathcal{C} along the photosphere, used to compute Γ_b . The photospheric plan view (right) shows the path \mathcal{C} as well as a path, \mathcal{C}^+ used to compute χ_+ inside \mathcal{F}_i^+ .

The scalar field $\chi(x, y)$ is a gauge field transforming the vector potential $\mathbf{A}^{(v)}$, defined, in eq. (4) by a line integral of $\mathbf{A} - \mathbf{A}^{(v)}$, along a photospheric path beginning at one particular point \mathbf{x}_0 . Because the horizontal curl of its integrand, $\hat{\mathbf{z}} \cdot \nabla \times [\mathbf{A} - \mathbf{A}^{(v)}]$, vanishes everywhere on the photosphere, the integral depends on its endpoints and not the choice of path between them. Assuming both footprints are simply-connected regions, we can make $\chi = \chi_+$ everywhere inside \mathcal{F}_i^+ by choosing $\mathbf{x}_0 = \mathbf{x}_+$. Within the other footprint χ will differ from χ_- by the constant

$$\Gamma_+^- \equiv \int_{\mathbf{x}_+}^{\mathbf{x}_-} [\tilde{\mathbf{A}}_i - \tilde{\mathbf{A}}_i^{(v)}] \cdot d\mathbf{l} = \underbrace{\int_{\mathbf{x}_+}^{\mathbf{x}_-} \tilde{\mathbf{A}}_i \cdot d\mathbf{l}}_{\Gamma_a} - \underbrace{\int_{\mathbf{x}_+}^{\mathbf{x}_-} \tilde{\mathbf{A}}_i^{(v)} d\mathbf{l}}_{\Gamma_b} , \quad (25)$$

where the integral is performed along some photospheric path outside the footprints, such as the path \mathcal{C} in fig. 5. Expression (23) follows from using $\chi = \chi_- + \Gamma_+^-$ in the \mathcal{F}_i^- portion of the surface integral in (3).

While the horizontal curls of both $\tilde{\mathbf{A}}_i$ and $\tilde{\mathbf{A}}_i^{(v)}$ vanish everywhere outside of the footprints, the fields themselves need not. The integrals Γ_a and Γ_b are therefore not zero, but they can be performed over different photospheric paths provided each path lies outside the footprints and they can be continuously deformed into one another without entering either footprint.

The right-most integral, Γ_b , can be evaluated using elements from previous steps. The unconfined field $\tilde{\mathbf{B}}_i^{(v)}$ and its vector potential, $\tilde{\mathbf{A}}_i^{(v)}$, were computed throughout \mathcal{V} in the course of finding T_2 . They are therefore known at every point in the photosphere and the line integral of $\tilde{\mathbf{A}}_i^{(v)}$ can be computed along some path connecting \mathbf{x}_+ to \mathbf{x}_- .

Even if we do not know $\tilde{\mathbf{A}}_i$ outside \mathcal{D}_i , we do know that its curl vanishes there. It follows from this that a line integral of $\tilde{\mathbf{A}}_i$ will not be changed as the path of integration is continuously deformed, provided the path remains outside the domain. In particular the integration path from Γ_a may be lifted off the photosphere and brought into contact, everywhere, with $\partial\mathcal{D}_i$. The vector potential $\tilde{\mathbf{A}}_i$ will be continuous across $\partial\mathcal{D}_i$, in spite of its surface current, so it will match \mathbf{A} , which we do know.

Using these facts we choose the integration path to be a field line, \mathcal{L}_o , from the boundary, $\partial\mathcal{D}_i$, as shown in fig. 5. This means we must choose \mathbf{x}_+ and \mathbf{x}_- to be its footprints (the footprints will lie on $\partial\mathcal{F}_i^+$ and $\partial\mathcal{F}_i^-$). The field line is found by selecting an initial point just inside the perimeter of \mathcal{F}_i^+ and tracing it until it ends just inside \mathcal{F}_i^- . The field line \mathcal{L}_o is traced using the field \mathbf{B} , since that matches $\tilde{\mathbf{B}}_i$ inside \mathcal{D}_i . As it is being traced the integral

$$\Gamma_a = \int_{\mathcal{L}_o} \mathbf{A} \cdot d\mathbf{l} , \quad (26)$$

is performed using the vector potential \mathbf{A} , since this also matches $\tilde{\mathbf{A}}_i$ inside the domain.

The calculation of Γ_a and Γ_b is more straightforward in the common situation that some portion of $\partial\mathcal{D}_i$ lies within the photosphere $z = 0$. This occurs where “photospheric domains” encounter field-free, i.e. $B_z = 0$, portions of the photosphere (Longcope & Klapper 2002), such as in the illustrative example of a constant- α field rooted in four sources. In cases such as this \mathcal{L}_o will lie in the photosphere, it can be initiated there and will terminate there. Both integrals for Γ_a and Γ_b will then be performed along this path. This is equivalent to performing the first integral in eq. (25) along the photospheric path, where $\tilde{\mathbf{A}}_i = \mathbf{A}$.

The complete calculation proceeds as follows. Perform the Monte Carlo integration of T_1 according to eq. (20), while finding the flux ψ_i at the same time, according to (21). Trace field lines from every pixel in each photospheric source region to identify the footprints \mathcal{F}_i^+ and \mathcal{F}_i^- . Use these to construct a magnetogram from which potential field $\tilde{\mathbf{B}}_i^{(v)}$ is extrapolated. Find its vector potential and calculate T_2 from eq. (22). Choose one point, \mathbf{x}_+ at the perimeter of \mathcal{F}_i^+ , and trace this field line, \mathcal{L}_o , to its opposite end; this is \mathbf{x}_- . Compute Γ_a , according to (26) while tracing the field line. Then compute Γ_b along some topologically equivalent photospheric path; this is a path, such as \mathcal{C} in fig. 5, which can be deformed into \mathcal{L}_o without crossing the photosphere or \mathcal{D}_i . Finally, construct the scalar fields χ_+ and χ_- within each footprint according to (24), by propagating the integrals from \mathbf{x}_\pm using the Haffa et al. (2006) algorithm. Integrate these according to (23) and add their sum to $-\psi_i(\Gamma_a - \Gamma_b)$ to find T_3 . The unconfined relative helicity is then $\tilde{H}_i = T_1 - T_2 + T_3$.

4.1.1. Example

Applying the method above to domain *P2-N1* from the quadrupolar constant- α field, gives the solid curve in fig. 6. The other curves show separately each of the three terms. Term two (dotted line) is relatively small because we used an approximation of expression (6) at the photosphere to produce $\tilde{\mathbf{A}}_i^{(v)}$; it is probably not exactly zero because of the influence of the upper boundary. The same kind of expression is used for the photospheric level of the vector potential $\mathbf{A}(\mathbf{x})$. The fact that T_3 is significantly different from zero demonstrates the differences between $\tilde{\mathbf{A}}_i$ and \mathbf{A} which must be compensated by $\chi(x, y)$.

The above description has emphasized the extent to which the individual terms used to compute the unconfined self-helicity depend on the specific method by which the vector potentials are found (i.e. on choice of gauge). The gauge-invariance of their sum, the helicity, is demonstrated by repeating the calculation at one value, $\alpha = -1/2$, after adding the gradients of different scalar fields to $\mathbf{A}(\mathbf{x})$ and $\tilde{\mathbf{A}}_i^{(v)}$ (gradients of $r^2/20$ and $xy/10$ respectively). The

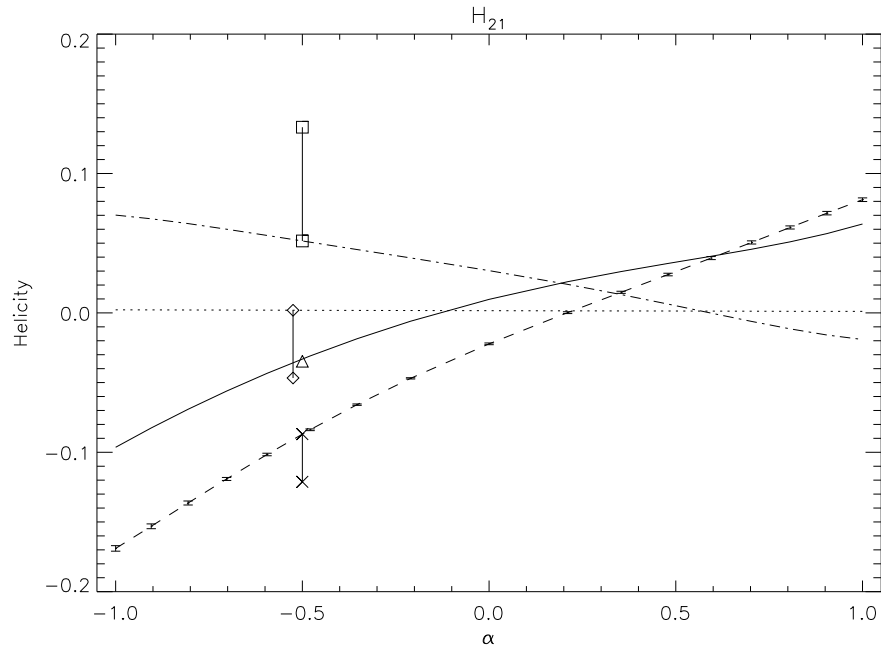


Fig. 6.— The variation in unconfined self-helicity of domain $P2-N1$ (solid) *vs.* α . Other lines show each term used in its calculation: T_1 (dashed), T_2 (dotted) and T_3 (broken). Error bars on T_1 show the statistical uncertainties from using a Monte Carlo method. Vertical bars connect each term to a symbol representing its value, at $\alpha = -1/2$, after each vector potential has been subject to a different gauge transformation. The triangle shows that their sum, lies on the solid line: its is gauge invariant.

values of terms found after this addition are marked by symbols and connected to symbols at the pre-transformation values by vertical lines. The gauge-transformation changes each term by a significant amount, but their sum (Δ) is not changed — the helicity is gauge-invariant, as it should be.

The algorithm was checked independently by computing \tilde{H}_i directly, by eq. (2) over \mathcal{V} , using a numerical version of the restricted field $\tilde{\mathbf{B}}_i$. This was computed by multiplying \mathbf{B} by a numerical version of the support function, Θ_i , found as described in the following section. The resulting helicity agreed with the sum of the three terms.

The unconfined self-helicity of three different domains are shown in fig. 7. The solid curves are distinguished by the same symbols as in fig. 4. Here \tilde{H}_{12} and \tilde{H}_{21} are identical due to symmetry, and so their symbols (triangles and diamonds) appear on the same line. The solid curve with squares shows the much smaller values of \tilde{H}_{11} . The curves are not symmetric about $\alpha = 0$, due in part to the behavior of the fluxes in each domain (see fig. 4). The flux of domain $P1-N1$ (ψ_{11}) increases with α , while fluxes in the other two decrease. Dashed lines are $\alpha\psi^2/2\pi$, illustrating that the fluxes alone lead to a similar asymmetry.

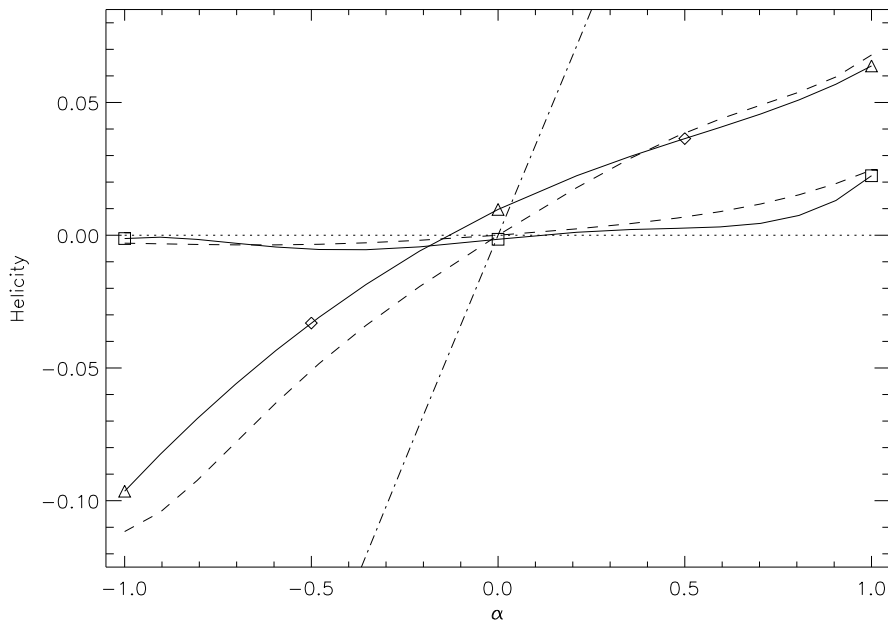


Fig. 7.— Plots of the unconfined self-helicities of three domains (solid curves). Domains are designated by the same symbols as in fig. 4: $P1-N1$, square, $P1-N2$, diamond; and $P2-N1$ triangle. Dashed curves show $\alpha\psi^2/2\pi$, for reference. The broken curve shows the relative helicity of the entire field.

It is also evident from fig. 7 that $\tilde{H}_{12} > 0$ for a potential field ($\alpha = 0$). It was predicted during its derivation, that the unconfined self-helicity might be non-zero even for a portion of a potential field. With this specific example in hand it is possible to understand the non-vanishing helicity using field lines from the restricted field, $\tilde{\mathbf{B}}_i$, and the unconfined field, $\tilde{\mathbf{B}}_i^{(v)}$, shown in fig. 8. In each case field lines are traced from the same equilateral triangle of points located in \mathcal{F}_{12}^- (diamonds). These end up at a triad of points in \mathcal{F}_{12}^+ . The expanded view on the left shows that the triad from the restricted field (squares) is rotated by approximately 5° relative to that from the unconfined field (triangles).

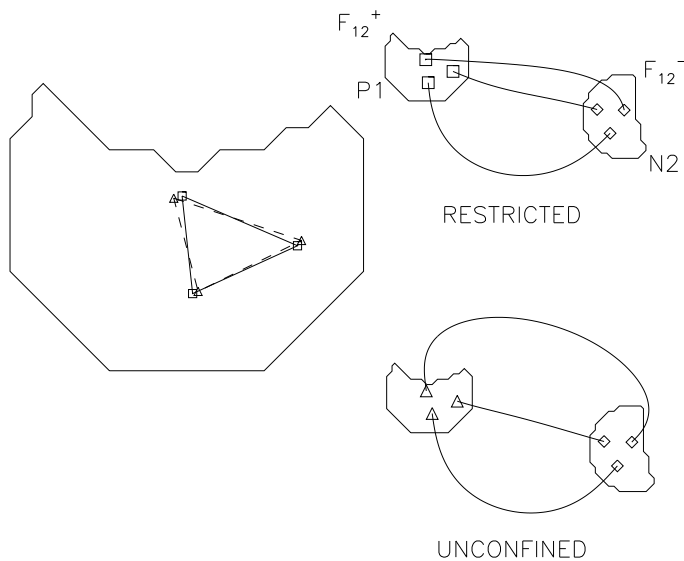


Fig. 8.— Field lines from the restricted field ($\tilde{\mathbf{B}}_i$, top right) and the unconfined field ($\tilde{\mathbf{B}}_i^{(v)}$, bottom right). In each case the field lines are started from the same equilateral triangle of points (diamonds) in \mathcal{F}_{12}^- . Their endpoints in \mathcal{F}_{12}^+ are indicated by triangles and squares for the two fields. These are superposed in the expanded view on the left.

To see how this rotation of footpoints leads to $\tilde{H}_{12} > 0$ consider the following process. Begin with the unconfined field, $\tilde{\mathbf{B}}_i^{(v)}$, whose photospheric field vanishes outside of the footprint regions, \mathcal{F}_{12}^\pm , but whose coronal field lines fill the entire volume (the lower field lines in fig. 8). Now consider continuously increasing the photospheric field outside these footprint regions until it matches the original field everywhere. The potential field overlying this increasing flux distribution will push its way into the volume, squeezing the field lines from domain $P1-N2$ into the volume they occupy in the restricted field. As they are squeezed into this volume their footpoints, the ones within \mathcal{F}_{12}^+ , appear to rotate in a clockwise sense.

This is the sense of rotation which will inject *positive helicity* into the coronal field. Thus, even though no currents were introduced, the field in domain $P1-N2$ has been “twisted” in a right-handed sense in the course of changing it from $\tilde{\mathbf{B}}_i^{(v)}$ to $\tilde{\mathbf{B}}_i$. This means the latter field has positive helicity relative to the former: $\tilde{H}_{12} > 0$.

4.2. Computing the additive self-helicity

Computation of the additive self-helicity requires the function $\Theta_i(\mathbf{x})$ to be found explicitly and that the field $\mathbf{P}_i(\mathbf{x})$ be found everywhere inside \mathcal{D}_i . These steps require more sophisticated, and computationally expensive, methods than the ones outlined in the previous section. Moreover, they are not steps otherwise performed in the calculation of relative helicity. Once these elements are found, however, the calculation is relatively straightforward.

The support function $\Theta_i(\mathbf{x})$ must be computed and somehow represented. The obvious representation is as an array on some computational grid. The array is one on every grid point determined to belong to \mathcal{D}_i , and zero elsewhere. In order to obtain this we begin with a magnetic field, $\mathbf{B}(\mathbf{x})$, assumed to be defined on the same grid. It is possible for the full volume, \mathcal{V} , to extend beyond the grid, but the grid must include the entire domain \mathcal{D}_i .

To populate the support function array, we trace field lines from \mathcal{D}_i and set to unity each grid point whose surrounding voxel is passed through. We have developed an algorithm for efficiently selecting field lines so that no erroneous gaps remain in Θ_i . The algorithm is not simple, so its details are described in an appendix. An example of its results produced the transparent volume in fig. 1b.

The reference field, $\mathbf{P}_i(\mathbf{x})$, satisfying eq. (13) within the domain must next be found. Proposing the form $\mathbf{P} = \nabla\varphi$, we seek a potential which is harmonic, $\nabla^2\varphi = 0$, within the domain. The potential must also satisfy homogeneous Neumann conditions, $\hat{\mathbf{n}} \cdot \nabla\varphi = 0$, on all boundaries, $\partial\mathcal{D}_i$, except the footprints, where $\partial\varphi/\partial z = B_z$.

The harmonic function, φ , is defined on the grid, and may be iteratively computed using a standard relaxation technique (Press et al. 1986). In each iteration the value of φ on a given grid point is replaced by the average of its neighbors. At a point adjacent to a point inside the domain, (i.e. on the boundary), its value is taken from the adjacent interior point. If the grid point is part of the footprint, its value is set to $\varphi(\Delta z) - \Delta z B_z$, where Δz is the vertical grid spacing. This step is alternated with relaxation, and the pair of steps are repeated until successive changes in φ are deemed small enough to indicate convergence. The gradient of the scalar potential on the entire grid is then computed and multiplied by Θ_i to yield \mathbf{P}_i on the same grid. More details of this method are given in an appendix.

Multiplying the full magnetic field \mathbf{B} by the support function array Θ_i yields a numerical version of the restricted field $\tilde{\mathbf{B}}_i$. From that array it is a straightforward matter to construct a vector potential $\tilde{\mathbf{A}}_i$ at every point on the computational grid. Applying an identical procedure to \mathbf{P}_i yields $\mathbf{A}_i^{(p)}$ on the grid. Neither of these vector potentials are guaranteed to vanish outside \mathcal{D}_i , however, their values there will not enter into the self helicity. Using the Finn-Antonsen integral, eq. (2), both vector potentials will be multiplied by a field, $\tilde{\mathbf{B}}_i - \mathbf{P}_i$, which vanishes outside the domain. The integral can be performed over the entire grid, to yield the additive self-helicity.

The additive self-helicity, $H_{21}^{(s)}$, of domain $P2-N1$ is plotted in fig. 9 for the quadrupole field with various values of α . Owing to the computational expense of the method, the values were calculated using a $60 \times 60 \times 30$ grid. The unconfined self-helicity, \tilde{H}_{21} , is plotted for reference. The two are quite similar in general, which is notable in light of the completely different methods used in their computation. The approximate value $H_{21}^{(s)} = 0$ at $\alpha = 0$ demonstrates the efficacy of the relaxation used to compute \mathbf{P}_i in this case. The solid curve, \tilde{H}_{21} , appears similar to $H_{21}^{(s)}$ shifted upward by the same constant everywhere.

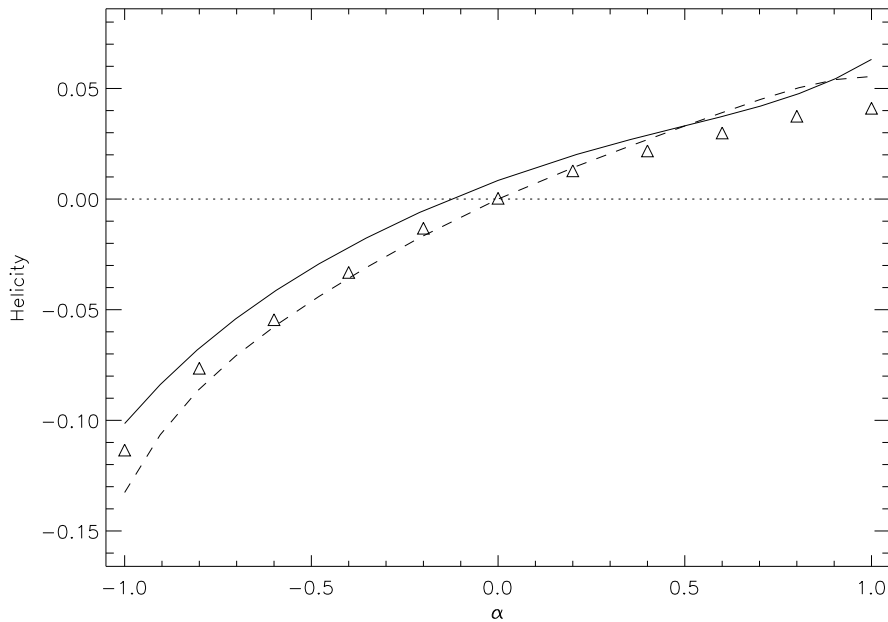


Fig. 9.— Plots of the additive self-helicities of domain $P2-N1$ (triangles) versus α . Also shown are the unconfined self helicity (solid line) and the empirical function eq. (27), as a dashed line

The dashed curve in fig. 9 shows an empirical function,

$$H_i^{(s)} = \frac{\alpha}{4\pi} \langle L \rangle_i \psi_i^2 , \quad (27)$$

where $\langle L \rangle_i$ is the average length of a field line in \tilde{B}_i . This formula would yield the twist helicity if the domain were a thin flux tube of length $\langle L \rangle$, with axial current density $J = \alpha B$. It provides a fairly good approximation of $H_{21}^{(s)}$.

5. Energy Bounds from Additive Self-Helicity

One of the most conceptually useful properties of additive self helicity arises from its use as a constraint. It is well known that minimizing magnetic energy subject to a constraint on a field's relative helicity results in a constant- α force-free field (Woltjer 1958; Taylor 1986). This fact is readily verified by substituting $\mathbf{A} + \delta\mathbf{A}$ into an energy functional consisting of the magnetic energy added to a relative helicity expression multiplied by an undetermined Lagrange multiplier $\alpha/8\pi$,

$$W\{\mathbf{A}\} = \frac{1}{8\pi} \int_{\mathcal{V}} |\nabla \times \mathbf{A}|^2 d^3x + \frac{\alpha}{8\pi} \left[H_R - \int_{\mathcal{V}} (\mathbf{A} + \mathbf{A}^{(v)}) \cdot \nabla \times (\mathbf{A} - \mathbf{A}^{(v)}) d^3x \right] . \quad (28)$$

The term in square brackets vanishes identically as long as the helicity constraint is observed. Variations in the vector potential, $\delta\mathbf{A}$, are arbitrary except that they cannot change the normal field at the boundary. This means that $\mathbf{A}^{(v)}$ does not change and $\delta\mathbf{A} \times \hat{\mathbf{n}} = 0$ on $\partial\mathcal{V}$. The latter fact facilitates the transformation of the energy functional using integration by parts, leaving first order variation

$$\delta W = \frac{1}{4\pi} \int_{\mathcal{V}} [\nabla \times \mathbf{B} - \alpha\mathbf{B}] \cdot \delta\mathbf{A} d^3x . \quad (29)$$

For the field $\mathbf{B}(\mathbf{x})$ to be an energy minimum, subject to the helicity constraint, this variation must vanish for any choice of $\delta\mathbf{A}(\mathbf{x})$, provided it vanishes at the boundary. This can only happen if the term in square brackets vanishes at every point, except possibly on the boundaries; it is a constant- α force free field. Here the uniformity (i.e. constancy) of α follows directly from its use as an undetermined multiplier for the entire relative helicity integral.

Minimization without invoking the helicity constraint is formally identical but without the undetermined multiplier. The first order variation resembles (29) but with $\alpha = 0$. Requiring this variation to vanish leads to the equation for a potential field $\nabla \times \mathbf{B} = 0$, demonstrating the potential field to be the unconstrained minimum energy state.

A series of steps identical to those above can be used to find the field within a domain \mathcal{D}_i with the minimum energy subject to a constraint on $H_i^{(s)}$. If the shape of the domain \mathcal{D}_i is held fixed during this minimization, the first order variation is identical to eq. (29) except that the integration is over \mathcal{D}_i . Thus the minimizing field has constant α within the domain.

The energy of the entire field can be minimized, subject to constraints on its self-helicities, by varying the functional

$$\sum_i \int_{\mathcal{D}_i} |\nabla \times \mathbf{A}|^2 + \sum_i \alpha_i \left[H_i^{(s)} - \int_{\mathcal{D}_i} (\mathbf{A} + \mathbf{A}_i^{(p)}) \cdot \nabla \times (\mathbf{A} - \mathbf{A}_i^{(p)}) d^3x \right] , \quad (30)$$

analogous to (28). The term on the left is identical to the standard energy integral (omitting the factors $1/8\pi$), since $\bigcup \mathcal{D}_i = \mathcal{V}$. Each of the terms in square brackets concerns a different domain, and will vanish if the field in that domain satisfies the constraint on its additive self-helicity. To enforce each constraint independently it is multiplied by its own undetermined multiplier, α_i . Since each integral is over only the domain \mathcal{D}_i it is unnecessary to use the restricted forms of the vector potential $\tilde{\mathbf{A}}_i$.

The energy functional in eq. (30), is equivalent to a sum of energy functionals for the fields within each domain separately. The minimizing field satisfies the equation

$$\nabla \times \mathbf{B} = \alpha_i \mathbf{B} \quad , \quad \mathbf{x} \in \mathcal{D}_i \quad , \quad (31)$$

which is a *piece-wise-constant- α field*, hereafter referred to as \mathbf{B}_{α_i} . Each domain has its own α_i , and the field is tangent to its boundaries. There might be additional surface currents at the boundaries $\cup_i \partial \mathcal{D}_i$. The values of α_i are found by matching the self-helicities. For small values of $H_i^{(s)}$ the relation must be linear

$$\alpha_i \simeq \frac{4\pi H_i^{(s)}}{\psi_i^2 \bar{L}_i} \quad , \quad (32)$$

where \bar{L}_i is a quantity with units of length depending on the geometry of the volume \mathcal{D}_i . The example in fig. 9, along with eq. (27), shows that $\bar{L}_i \simeq \langle L \rangle_i$ the flux-averaged field line length within the domain.

The variation within each domain without constraining the helicity is, again, formally identical but without the undetermined multipliers: $\alpha_i = 0$. Note that this version of the variation preserves all of the domains and their shapes. The Euler-Lagrange equations are therefore (31) with $\alpha_i = 0$. These are the equations for \mathbf{P}_i , which combine into the field $\mathbf{P}(\mathbf{x})$ according to eq. (13). This is therefore the field which minimizes energy subject to constraints on the shapes of all domains.

The piece-wise constant- α field has the same domains with the same shapes and the same self-helicities as the original field \mathbf{B} . It is, however, the field with the minimum energy sharing these properties. The field $\mathbf{P}(\mathbf{x})$ has the same domains and shapes but with no constraint on their self-helicities. Eliminating a constraint will always produce a field whose minimum energy is no larger. This means that the energies of these fields satisfy the inequalities

$$W\{\mathbf{B}\} \geq W\{\mathbf{B}_{\alpha_i}\} \geq W\{\mathbf{P}\} \geq W\{\mathbf{B}^{(v)}\} . \quad (33)$$

The traditional constant- α field cannot be placed into this hierarchy since the relative helicity of the entire field is not simply related to its self-helicities alone. In particular, it is not equal to the sum of self-helicities owing to possible mutual helicity as in eq. (16). The constant- α field is a special case of a piece-wise-constant- α field, but with $\alpha_i = \alpha$ in each domain. Its domains will not, however, conform to those of the original field \mathbf{B} . So while its energy is guaranteed to be no larger than $W\{\mathbf{B}\}$ and no smaller than $W\{\mathbf{B}^{(v)}\}$, it cannot be related to $W\{\mathbf{B}_{\alpha_i}\}$ in general.

The flux constrained equilibrium (FCE) introduced by Longcope (2001), hereafter denoted $\mathbf{B}^{(f)}$, fits naturally into the above hierarchy of magnetic energies. The FCE corresponding to the original field $\mathbf{B}(\mathbf{x})$ has equivalent domains with the same fluxes, ψ_i , but not necessarily the same shapes. It is the field of least energy with those specified domain fluxes. Since the shapes of the domain are not constrained, these are a subset of the constraints to which \mathbf{P} was subject. It therefore follows that

$$W\{\mathbf{B}\} \geq W\{\mathbf{B}_{\alpha_i}\} \geq W\{\mathbf{P}\} \geq W\{\mathbf{B}^{(f)}\} \geq W\{\mathbf{B}^{(v)}\} . \quad (34)$$

It has been shown by Longcope (2001) that $\mathbf{B}^{(f)}$ is current-free except for singular current sheets confined to *separators* — domain boundaries which adjoin curves along which three domains meet. This contrasts with the structure of \mathbf{P} which has current sheets along *separatrices*, where two domains meet (essentially boundaries $\partial\mathcal{D}_i$). As a result of the less restrictive constraints on it $\mathbf{B}^{(f)}$ has current sheets on fewer locations. With no restrictions on their shapes the domains deform in order to lower their collective energy. This deformation leads to the formation of separator ribbons anywhere that four domains meet in $\mathbf{B}(\mathbf{x})$ (Longcope 2001). The net currents flowing on each of these separators, I_σ , may be estimated from the complete set of domain fluxes ψ_i (Longcope & Magara 2004).

All the domains of $\mathbf{B}^{(f)}$ are current-free so they have zero self-helicity (i.e. additive self-helicity). Its relative helicity can be approximated to lowest order in the separator currents I_σ of all its separators

$$H_R^{(f)} = H(\mathbf{B}^{(f)}|\mathbf{B}^{(v)}) \simeq \sum_{\sigma} I_{\sigma} \int_{c_{\sigma}^{(v)}} \mathbf{z}^{(v)} \cdot d\mathbf{l} , \quad (35)$$

where $\nabla \times \mathbf{Z}^{(v)} = \mathbf{A}^{(v)}$, and $\mathcal{C}_\sigma^{(v)}$ follows the separator of the potential field, and closing along the photosphere (Longcope & Magara 2004). This is naturally the *mutual helicity* of $\mathbf{B}^{(f)}$. It is not, however, the mutual helicity of \mathbf{P} , since that has domains of different shape.

6. Discussion

The foregoing has shown that there are least two different ways to compute the helicity contained in a given portion of a magnetic field. each is a logically self-consistent generalization of the original relative helicity of Berger & Field (1984). In many situations the methods yield different values, so they are not simply different expressions of the same underlying quantity. Indeed, each has its own advantages and disadvantages, and each will probably prove to be the best one for some task.

The unconfined self-helicity, \tilde{H}_i , is defined relative to a reference field, $\tilde{\mathbf{B}}_i^{(v)}$ which fills all of space (i.e. \mathcal{V}) even though the field in question, $\tilde{\mathbf{B}}_i$, does not. It turns out to be slightly easier to compute in practice. We presented one method which, while not straight-forward, can be implemented for magnetic fields defined in a wide range of ways.

The additive self-helicity, $H_i^{(s)}$, is defined relative to a field, \mathbf{P}_i , occupying the same volume as the field in question and defined to be current-free within that volume. While conceptually simple, finding the volume can be cumbersome in some circumstances, since it depends on the magnetic field itself. Moreover, it is necessary to compute a potential field within the irregular volume subject to conditions on all of its complicated boundaries.

Some differences between the self-helicities are evident from their definition. For example, if the field in question, $\tilde{\mathbf{B}}_i$, was extracted from a potential field, then $H_i^{(s)} = 0$, while this is not true of \tilde{H}_i . The additive helicity therefore preserves some of the energetic utility of relative helicity: a non-zero value implies a non-zero self-energy. This reasoning can be extended to show that the state of minimum energy, subject to constraints on all \tilde{H}_i , is a piece-wise constant- α field \mathbf{B}_{α_i} . Such a field falls in a hierarchy of magnetic fields of decreasing energies, arising from minimization subject to fewer constraints.

The additive self-helicity is additive in the sense that summing the self-helicity of neighboring domains, \mathcal{D}_{i1} and \mathcal{D}_{i2} , yields a relative helicity for the composite domain $\mathcal{D}_i = \mathcal{D}_{i1} \cup \mathcal{D}_{i2}$. The resulting helicity is relative to $\mathbf{P}_{i1} + \mathbf{P}_{i2}$, rather than to \mathbf{P}_i . The difference is the mutual helicities of the two domains.

Some previous studies of flux tubes, such as magnetic clouds, have used a helicity defined according to what we herein call additive self helicity (Rust & Kumar 1994; Dasso et al. 2003).

Magnetic clouds consist of twisted flux confined to a long, slender volume such as a cylinder. Their helicity, when it has been computed, is found with reference to untwisted flux confined to the same volume. This reference field is \mathbf{P}_i for the volume, so the helicity defined this way is $H_i^{(s)}$.

When used on flux confined to a thin tube the additive self helicity turns out to be equal to the *twist helicity* of the flux tube (Berger & Field 1984; Moffatt & Ricca 1992). The decomposition into twist and writhe invokes, as a reference, an untwisted magnetic field confined to the tube. It is possible to define twist and writhe for thin tubes anchored to a boundary (Berger & Prior 2006). The writhe helicity of the tube is the helicity of this reference field (defined with reference to another field). The twist helicity alone is not a topological invariant since it will change as the tube is deformed, even though the field inside undergoes no topological changes (i.e. it evolves ideally).

The additive self-helicity is defined for domains of any shape, including but not restricted to, a thin tube. As such it can be considered a generalization of the twist helicity to volumes other than thin tubes. It shares with twist helicity a lack of topological invariance, due to a dependence, through, \mathbf{P}_i , on the shape of its volume. It is, however, invariant to any ideal, internal motions which do not deform the volume.

The unconfined self-helicity, on the other hand, is preserved under any ideal plasma motions, provided they are *internal* (the boundary is fixed). The unconfined potential field, which depends only on the normal flux distribution at the boundary, will not be changed by such motions. The unconfined self-helicity of a flux tube will not change even as the flux tube undergoes a kinking motion which changes its twist and writhe. Such a definition was tacitly used by Fan & Gibson (2004) to compute the self-helicity of the kinking flux rope in their simulation.

It is not clear how different the two helicities will be in typical solar circumstances. In certain cases, such as volumes and footprints with perfect reflectional symmetry, the two will be identical. In our quadrupolar, constant- α example field, they turned out to differ only slightly (but they were demonstrably different). The volume in question was not reflectionally symmetric, but did not depart from symmetry as dramatically as a writhed thin tube might. Thus it is possible that the difference between the two helicities will be more significant in principle than in practice.

One distinction lies in the usefulness of one, the additive self helicity, as a constraint. Minimization subject to these constraints yields a piece-wise constant- α field of the kind invoked in the past owing to properties superior to genuine constant- α fields. Here we demonstrate how they arise from constrained minimization. The unconfined self-helicities,

on the other hand, are defined in overlapping volumes and cannot be used in a similar fashion as constraints.

In the final analysis, though, it would seem then that there is no single, universally useful, definition of self-helicity. We have chosen to explore the two forms that seem most natural, and that have appeared tacitly in previous investigations. It seems that the application will dictate which of these two helicities is the appropriate one for a given purpose.

We thank Yuhong Fan, B.C. Low and Sarah Gibson for useful discussions and e-mail correspondence on this subject. This work was funded by NSF grant ATM-0416340.

A. Finding the domain support function

The computation of additive self-helicity requires the support function for a given domain, $\Theta(\mathbf{x})$, be represented on the same grid as the magnetic field. (We have dropped the subscript designating the domain, since support functions are computed for one domain at a time.) The support function is computed by an algorithm taking as inputs the gridded field itself, and a photospheric array, called the boundary mask. The latter array designates the positive and negative regions which will be at the footpoints of each field line in \mathcal{D} : the array is one on each of these pixels and zero elsewhere. The simplest method of constructing the support function would be to trace a field line in both direction from every voxel in the computational grid, and set $\Theta = 1$ in the voxel if the footpoints both terminate in pixels from the boundary regions, and set $\Theta = 0$ otherwise.

We have developed an algorithm which is, in principle, more efficient than the simple one because it traces field lines from only a subset of voxels. It works by progressively adding voxels to Θ at the edges of those already known to belong to \mathcal{D} . We add a voxel, $\mathbf{r}_{i,j,k}$ under two different circumstances. 1. A field lines initialized somewhere within $\mathbf{r}_{i,j,k}$ is found to have both footpoints within the boundary mask. 2. A field line initiated in some other voxel, and determined to belong to \mathcal{D} , passes through some portion of $\mathbf{r}_{i,j,k}$.

The algorithm proceeds in three stages. First, a primary search traces field lines from each pixel in the boundary mask. If the field line is found to end at the other mask region, we add to the growing function, Θ , all voxels passed through by that field line (see left of fig. 10). A secondary search then checks each voxel neighboring those in Θ , adding any satisfying either criteria above. As voxels are found to belong to \mathcal{D} they are removed from the list of eligible voxels. Those found not to belong are added to a list of ineligible voxels. After one iteration, new boundary voxels are identified and the secondary search is repeated on those

still considered eligible. The iteration continues until every boundary voxel of Θ appears on the ineligible list. Finally, a tertiary search looks for voxels marked ineligible, but actually having a small portion within \mathcal{D} . This requires field lines to be traced from all corners of certain voxels.

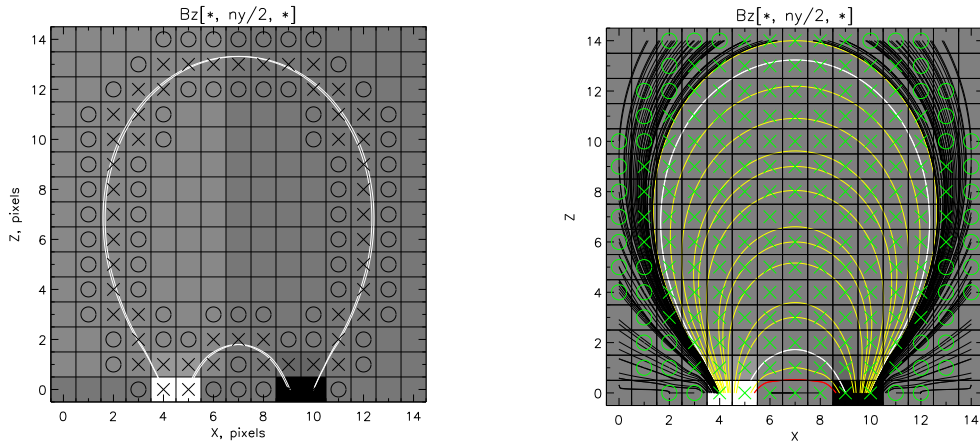


Fig. 10.— Stages in the growth of the support function Θ , illustrated using a simple dipole, whose footpoints (marked with white and black squares) are the boundary mask regions. In this illustration field lines cross the outer boundaries, but these excluded from \mathcal{D} . Plots show a cut through the middle of the dipole. (left) Field lines (solid white) from the primary search are initiated in each of the boundary pixels. Voxels found to belong to \mathcal{D} are marked with crosses, and their neighboring voxels with circles. (right) Voxels from the final Θ are marked with green crosses and those excluded are marked with circles. Solid curves show all field lines traced in the process of growing Θ . Black lines were found not belong to \mathcal{D} while yellow and red lines do belong to.

B. Finding the confined potential field

The confined potential field \mathbf{P} is curl-free within \mathcal{D} and tangent to the normals of $\partial\mathcal{D}$, except at the photosphere. We compute this field by defining $\mathbf{P} = \nabla\varphi$ and solving $\nabla^2\varphi = 0$ with Neumann conditions on $\partial\mathcal{D}$. In particular we impose

$$\left. \frac{\partial\varphi}{\partial n} \right|_{\partial\mathcal{D}, z \neq 0} = 0 \quad , \quad \left. \frac{\partial\varphi}{\partial z} \right|_{\mathcal{F}^\pm} = B_z \quad . \quad (\text{B1})$$

Due to the complex shape of \mathcal{D} , it is the most convenient to use relaxation, such as by Jacobi’s method (Press et al. 1986), to iteratively compute φ . In each iteration φ is replaced by an average of its neighbors. After an iteration, values of φ exterior to the irregularly shaped

domain are reset to satisfy conditions (B1). To simplify our discussion we will assume the grid is uniform and cubic: $\Delta x = \Delta y = \Delta z$.

For the most accurate representation of the boundary we found it necessary to use a staggered mesh, with the scalar potential placed at the centers of voxel faces while all three components of \mathbf{B} are located at the voxel center (see fig. 11). This staggering demands rather complicated averaging scheme since the 12 neighbors lie at varying distances from a given central face. The 13-point averaging kernel, illustrated in fig. 11, involves four faces with the same orientation, four each from the other two orientations, as well as the central face itself. In order to approximate the Laplacian to second order in grid spacing, faces parallel to the central face are given weights one-half that of the others. The Courant-Friedrichs-Lewy condition is satisfied, and the relaxation converges, if the central face is included in the average with a weight of $\frac{1}{6}$, parallel faces are given weights of $\frac{1}{24}$, and the other eight faces are each given a weight of $\frac{1}{12}$. Since the kernel involves fields from all kinds of faces it is immune to instabilities of the so-called “checkerboard” type (Press et al. 1986).

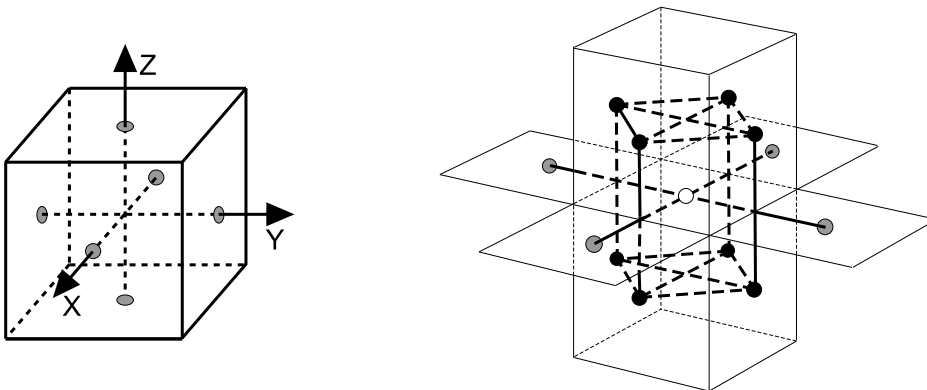


Fig. 11.— The staggered mesh used for computing the confined potential field. (left) The voxel faces on which the scalar potential is represented are designated by grey circles. (right) The neighboring faces which contribute to the average for a given face (white). In this example the central face is horizontal and its neighbors include 4 horizontal faces (grey) and eight vertical faces (black). The relaxation method involves replacing the value at the center with a weighted average of all 13.

Boundary conditions (B1), can be implemented for each local boundary configuration possible within the complex boundary surface. An example of the simplest configuration is an interior boundary voxel $\mathbf{r}_{i,j,k}$ with a single exterior neighbor, say $\mathbf{r}_{i+1,j,k}$. In this case the outward surface normal is $\hat{\mathbf{x}}$, and boundary condition (B1) is implemented by setting

$$\varphi^{(x)}(i + \frac{1}{2}, j, k) = \varphi^{(x)}(i - \frac{1}{2}, j, k) \quad , \quad (\text{B2})$$

where the superscript designates the face on which the variable is placed.

The staggering allows each of the possible surface normals to be treated. If the interior voxel, $\mathbf{r}_{i,j,k}$, considered above also abuts a second exterior voxel at $\mathbf{r}_{i,j+1,k}$ then the surface normal is parallel to $\hat{\mathbf{x}} + \hat{\mathbf{y}}$. In this case the boundary condition is

$$\varphi^{(x)}(i + \frac{1}{2}, j, k) = \varphi^{(y)}(i, j - \frac{1}{2}, k) \quad , \quad \varphi^{(y)}(i, j + \frac{1}{2}, k) = \varphi^{(x)}(i - \frac{1}{2}, j, k) \quad , \quad (\text{B3})$$

so that $(\hat{\mathbf{x}} + \hat{\mathbf{y}}) \cdot \nabla\varphi = 0$ when computed by centered differences. If the voxel were at a corner, and abutted the two exterior voxels above as well as $\mathbf{r}_{i,j,k+1}$, then the surface normal would be parallel to $\hat{\mathbf{x}} + \hat{\mathbf{y}} + \hat{\mathbf{z}}$. In this case we set

$$\varphi^{(x)}(i + \frac{1}{2}, j, k) = \frac{1}{2}\varphi^{(y)}(i, j - \frac{1}{2}, k) + \frac{1}{2}\varphi^{(z)}(i, j, k - \frac{1}{2}) \quad , \quad (\text{B4})$$

and similarly for $\varphi^{(y)}$ and $\varphi^{(z)}$ through cyclic permutation, in order that $(\hat{\mathbf{x}} + \hat{\mathbf{y}} + \hat{\mathbf{z}}) \cdot \nabla\varphi = 0$ at the voxel center.

Once the relaxation has converged the components of magnetic field vectors, \mathbf{P} , are computed using centered differencing in each voxel. Thus P_x is found from a difference of $\varphi^{(x)}$ and so forth. The result will be curl-free because it is the gradient of a scalar, and divergence-free because the scalar field satisfies Laplace's equation.

REFERENCES

- Bellan, P. M. 2000, *Sheromaks: A practical application of magnetohydrodynamic dynamos and plasma self-organization* (Imperial College Press)
- Berger, M. A. 1984, *Geophys. Astrophys. Fluid Dynamics*, 30, 79
- Berger, M. A. 1999, in *Geophysical Monograph*, Vol. 111, *Magnetic Helicity in Space and Laboratory Plasmas*, ed. M. R. Brown, R. C. Canfield, & A. A. Pevtsov (Washington, DC: AGU Press), 1
- Berger, M. A., & Field, G. B. 1984, *JFM*, 147, 133
- Berger, M. A., & Prior, C. 2006, *J. Math. Phys. A.*, 39, 8321
- Chae, J. 2001, *ApJ*, 560, L95
- Chae, J., Moon, Y.-J., & Park, Y.-D. 2004, *Solar Phys.*, 223, 39
- Chae, J., Wang, H., Qiu, J., Goode, P. R., Strous, L., & Yun, H. S. 2001, *ApJ*, 560, 476

- Dasso, S., Mandrini, C. H., Démoulin, P., & Farrugia, C. J. 2003, *JGR*, 108, 3
- Démoulin, P., & Berger, M. A. 2003, *Solar Phys.*, 215, 203
- Démoulin, P., Mandrini, C. H., van Driel-Gesztelyi, L., Thompson, B. J., Plunkett, S., Kovári, Z., Aulanier, G., & Young, A. 2002, *A&A*, 382, 650
- Démoulin, P., Pariat, E., & Berger, M. A. 2006, *Solar Phys.*, 233, 3
- DeVore, C. R. 2000, *ApJ*, 539, 944
- Fan, Y., & Gibson, S. E. 2004, *ApJ*, 609, 1123
- Finn, J., & Antonsen, T. M., Jr. 1985, *Comments Plasma Phys. Controlled Fusion*, 9, 111
- Hafla, W., Buchau, A., & Rucker, W. M. 2006, *Adv. Radio Science*, 4, 59
- Kusano, K., Maeshiro, T., Yokoyama, T., & Sakurai, T. 2002, *ApJ*, 577, 501
- Longcope, D., Beveridge, C., Qiu, J., Ravindra, B., Barnes, G., & Dasso, S. 2007, *Solar Phys.* (in press)
- Longcope, D. W. 2001, *Phys. Plasmas*, 8, 5277
- Longcope, D. W., & Klapper, I. 2002, *ApJ*, 579, 468
- Longcope, D. W., & Magara, T. 2004, *ApJ*, 608, 1106
- Longcope, D. W., Ravindra, B., & Barnes, G. 2007, *ApJ*, 668 (in press)
- Longcope, D. W., & Welsch, B. T. 2000, *ApJ*, 545, 1089
- Low, B. C. 1994, *Physics of Plasmas*, 1, 1684
- Low, B. C. 1996, *Solar Phys.*, 167, 217
- Low, B. C. 2006, *ApJ*, 646, 1288
- Low, B. C. 2006, *ApJ*, 649, 1064
- Melrose, D. 2004, *Solar Phys.*, 221, 121
- Moffatt, H. K., & Ricca, R. L. 1992, *Proc. Roy Soc. Lond. A*, 439, 411
- Nindos, A., Zhang, J., & Zhang, H. 2003, *ApJ*, 594, 1033
- Pariat, E., Démoulin, P., & Berger, M. A. 2005, *A&A*, 439, 1191

- Press, W. H., Flannery, B. P., Teukolsky, S. A., & Vetterling, W. T. 1986, *Numerical Recipes: The art of scientific computing* (Cambridge: Cambridge University Press)
- Régnier, S., Amari, T., & Canfield, R. C. 2005, *A&A*, 442, 345
- Rust, D. M., & Kumar, A. 1994, in *ESA SP-373: Solar Dynamic Phenomena and Solar Wind Consequences, the Third SOHO Workshop*, ed. J. J. Hunt, Vol. 3, 39
- Seehafer, N. 1978, *Solar Phys.*, 58, 215
- Taylor, J. B. 1974, *Phys. Rev. Lett.*, 33, 1139
- Taylor, J. B. 1986, *Rev. Mod. Phys.*, 58, 741
- Welsch, B. T., & Longcope, D. W. 2003, *ApJ*, 588, 620
- Wolfson, R., Vekstein, G. E., & Priest, E. R. 1994, *ApJ*, 428, 345
- Woltjer, L. 1958, *Proc. Nat. Acad. Sci.*, 44, 489
- Zhang, M., Flyer, N., & Low, B. C. 2006, *ApJ*, 644, 575